A-Site Vacancy Engineering in KNbO 3 Perovskite for Enhanced Lithium Storage

Abbas Khan, Eric Quarez, Nicolas Dupré, Eric Gautron, Andrea Balducci, Olivier Crosnier, Thierry Brousse

CHEMISTRY OF MATERIALS

pubs.acs.org/cm

Article

A-Site Vacancy Engineering in $KNbO_3$ Perovskite for Enhanced Lithium Storage

Abbas Khan, Eric Quarez, Nicolas Dupré, Eric Gautron, Andrea Balducci, Olivier Crosnier, and Thierry Brousse*

Cite This: *Chem. Mater.* 2025, 37, 3100−3112

Read Online

ACCESS | Metrics & More | Article Recommendations | Supporting Information

ABSTRACT: Design of tailored materials using innovative approaches that allow faster charging/discharging processes could be the key for improvement of electric mobility. In this work, a strategy is developed to modify $KNbO_3$ perovskite structure by partially substituting K^+ with La^{3+} at the A-site of the structure, creating two cation vacancies per substitution in the lattice. Materials with the general formula $K_{1-3x}La_x\square_{2x}NbO_3$ (with $0 \leq x \leq 0.15$; $\square$ is an A-site vacancy) have been synthesized by the sol−gel method. With La substitution and creation of artificial vacancies in the structure, $KNbO_3$ became activated for Li^+ insertion. The highly substituted $K_{0.55}La_{0.15}\square_{0.30}NbO_3$ (30% atomic A-site vacancies) exhibited 164 mAh g^{-1} at 0.02 A g^{-1} in the 0.05−3.0 V vs Li^+/Li potential window. *Ex situ* ^7Li and ^{93}Nb MAS NMR confirmed an increased Li^+ insertion in relation to vacancies and corresponding changes in Nb^{5+} local environment, respectively. *In situ* X-ray diffraction (XRD) analysis revealed a solid-solution-type storage mechanism with a maximum volume change of only 1.3% upon Li^+ insertion for highly substituted material. This accounts for the remarkable capacity retention obtained after 900 cycles at 0.1 A·g^{-1}. Diverged from the classical design of insertion materials, this study presents an alternative approach of creating vacancies without sacrificing the pristine phase, with a possibility to use the not so common class of ABO_3-type perovskites as the battery electrode.

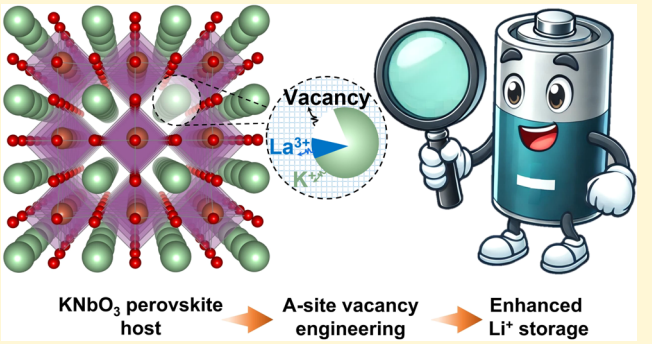

1. INTRODUCTION

The advancement of electric vehicles demands electrode materials that allow faster charge/discharge rates in Li-ion batteries (LIBs) through innovative designs and strategies.[1,2] Graphite, being the commercially known negative electrode material for LIBs, has major issues against fast charging. It has an average lithiation potential of approximately 0.1 V vs Li^+/Li, which poses a risk of lithium plating at high current rates, potentially leading to a short circuit in battery cell.[3,4] In this regard, spinel $Li_4Ti_5O_{12}$ (LTO) has been successfully implemented as an alternative to graphite for fast-charging applications. It can reversibly store Li^+ in the structure at a quite high average potential of 1.55 V vs Li^+/Li, while exhibiting nearly zero-strain characteristics.[5,6] Recently, Nb-based Wadsley-Roth phases with 3D open structures such as $TiNb_2O_7$,[7] $Nb_{16}W_5O_{55}$,[8] and PNb_9O_{25}[9] have gained great interest as high-power negative electrodes owing to their fast kinetics, robust ion diffusion, and good structural stability. Among other transition metal oxides with open crystallographic structures, ReO_3 pseudoperovskite stands out, delivering a specific capacity of 228 mAh·g^{-1} thanks to 2 Li^+ insertion per cation.[10]

However, Li^+ insertion into the corner-shared $[ReO_6]$ octahedra structure induces significant volume changes due to octahedral distortions, leading to low cyclability.

To relieve the lattice strain induced upon Li^+ insertion and avoid structural collapse in BO_3-type structures, ABO_3-type perovskites have emerged as an interesting choice. While the A-site atom in the center of the perovskite cage enhances structural stability, the fully occupied crystallographic sites limit Li^+ storage capacity. Among such perovskites, $La_{1/3}NbO_3$, $Pr_{1/3}NbO_3$, and $Ce_{1/3}NbO_3$ are notable examples that stabilize intrinsically with A-site deficiency and have been studied recently as negative electrodes for LIBs.[11−13] These materials leverage the redox activity of niobium ($Nb^{5+}/Nb^{4+}/Nb^{3+}$) upon Li^+ insertion into vacancies, enabling a robust pseudocapacitive mechanism. The insertion/desertion of Li^+ in A-site vacancies is compensated by tilting of $[NbO_6]$

Received: November 13, 2024
Revised: April 2, 2025
Accepted: April 3, 2025
Published: April 16, 2025

octahedra, preventing a large volume change.[14] However, insertion of Li^+ in the 3c-sites of the structure (at lower potentials of 0.8 V vs Li^+/Li) causes a significant decay of capacity over the cycles due to irreversible structural transformation around the Nb−O bond.[15] This motivated us to explore A-site doping to enhance the structural stability during deep Li^+ insertion.

Our group recently demonstrated a different strategy to tailor ABO_3-type perovskite structure, by partially substituting the A-site to create vacancies, thus activating the structures for Li^+ insertion. Based on the general formula $Ag_{1-3x}La_x\square_{2x}NbO_3$, (with $x \leq 0.20$; where $\square$ is an A-site vacancy), model materials were designed that allow fast Li^+ insertion following a solid-solution-type mechanism.[16] The highly substituted ($x = 0.15$) material achieved a maximum specific capacity of 35 mAh g^{-1} at a scan rate of 0.1 mV s^{-1}, with 95% capacity retention after 800 cycles within a potential window of 1.2−3.0 V vs Li^+/Li. Moreover, during charge/discharge at a constant current of 2 A g^{-1}, the capacity is still 30 mAh g^{-1}. However, these structures have quite a narrow-stability potential window primarily due to silver cation (Ag^+) sensitivity toward external stimuli.[17] Subsequently, we intended to transfer the concept from the model $AgNbO_3$ structure to a more cost-effective and abundantly available $KNbO_3$. To the best of our knowledge, this material has never been investigated as an LIB electrode.

$KNbO_3$ has been widely studied as a lead-free ferroelectric, piezoelectric, and electro-optic perovskite material.[18−20] Cation doping in the structure was reported to significantly enhance the structural and functional properties. For example, monovalent Li^+ or Na^+, divalent Ca^{2+}, and trivalent Sm^{3+} substitutions at the A-site of the structure have been reported previously.[21−24] While monovalent dopants induce strains in the structure due to size mismatch and favor a phase stabilization, di- or trivalent dopants require an additional charge compensation. Notably, in most of the cases, charge compensation has been reported because of oxygen vacancies. Specifically, Dudhe et al. studied the cubic-orthorhombic phase transition in $KNbO_3$ by varying oxygen vacancies through La-doping at the A-site.[25] However, the effect of substitution-dependent cation vacancies on the structure of $KNbO_3$ has rarely been examined.

In the present study, we propose a strategy to create A-site vacancies in $KNbO_3$ by partial substitution of K^+ with La^{3+} according to the general formula $K_{1-3x}La_x\square_{2x}NbO_3$ (with $0 \leq x \leq 0.15$; $\square$ is an A-site vacancy). Pure-phase compounds were synthesized by the sol−gel method. In-depth analysis of the effect of cation substitutions on the structure was done through X-ray diffraction refinements coupled with observation of microstructural changes. Subsequently, the effect of A-site vacancies on Li^+ storage behavior was investigated at different degrees of substitution. The compounds with vacancies exhibited a solid-solution-type mechanism upon lithiation with low volume expansion, which leads to a good cycling stability of $K_{1-3x}La_x\square_{2x}NbO_3$ electrodes.

2. EXPERIMENTAL SECTION

2.1. Material Synthesis. $K_{1-3x}La_x\square_{2x}NbO_3$ perovskites were synthesized by the sol−gel route as reported previously for perovskite materials.[16] Stoichiometric amounts of potassium nitrate (KNO_3 by Alfa Aesar, 99.9%), lanthanum nitrate hexahydrated ($La(NO_3)_3 \cdot 6H_2O$ by Sigma-Aldrich, 99.99% trace metals basis), and niobium(V) ammonium oxalate hydrate ($C_4H_4NNbO_9 \cdot xH_2O$ by Sigma-Aldrich, 99.99% trace metals basis) were dissolved in 30 mL of 30% (w/w) H_2O_2 in deionized (DI) water (Sigma-Aldrich) and stirred at room temperature. H_2O_2 serves as an oxidizing agent to stabilize cations. Citric acid monohydrated ($HOC(COOH)(CH_2COOH)_2 \cdot H_2O$ by Sigma-Aldrich, ≥98% GC/titration) was added to the solution in 2:1 cation molar ratio and stirred until a transparent solution was obtained. Citric acid acted as a complexing agent, of which the carboxyl and hydroxyl groups were occupied by K^+ and Nb^{5+}, respectively, through chelation reaction and prevented phase segregation. Although citric acid can act as a reducing agent, its interaction with H_2O_2 is kinetically limited under the synthesis conditions, and the excess H_2O_2 suppresses any redox reactions. The pH of the reaction was adjusted to 6.5 by adding ammonium hydroxide (NH_3(aq), Sigma-Aldrich). The pH adjustment facilitates gelation and stabilizes the chelated complexes. The solution was heated to 90 °C while stirring. Wet gel was obtained and converted to xerogel when kept in oven at 250 °C. The final materials were obtained by grinding xerogel and annealing at 600 °C in air for 2 h. The samples with varied La content were prepared and named as pristine $KNbO_3$, $K_{0.85}La_{0.05}\square_{0.10}NbO_3$, $K_{0.70}La_{0.10}\square_{0.20}NbO_3$, $K_{0.55}La_{0.15}\square_{0.30}NbO_3$, and $K_{0.40}La_{0.20}\square_{0.40}NbO_3$. A schematic illustration of synthesis route is presented in Figure S1.

2.2. Physical Characterizations. XRD measurements were performed on powder samples using a PANalytical X'Pert Pro-diffractometer (Malvern Panalytical, Almelo, Netherlands) with Cu−Kα_1−Kα_2 (λ = 1.54060, 1.54443 Å) radiation source and an acceleration voltage of 40 kV at a current of 40 mA. Data were recorded in the 2 theta range of 20−80°. For *in situ* XRD measurements, a Swagelok-type cell with beryllium window on top was used. The data were collected at the 2θ range between 20 and 70°. The Brunauer−Emmett−Teller (BET) specific surface areas of powders were calculated using N_2 adsorption−desorption isotherms at 77 K with a Quantachrome Nova 4200e equipment (Anton Paar). The scanning electron microscopy (SEM) of powders and cycled electrodes and energy-dispersive X-ray spectroscopy (EDX) were performed by Zeiss MERLIN Instrument using an in-lens annular detector at an operating voltage of 20 kV. To prepare the samples, a small fraction of the powder/electrode was stuck on a carbon tape. *Ex situ* ^{7}Li and ^{93}Nb MAS NMR experiments were done on a Bruker Avance-500 spectrometer (B_0 = 11.75T). Larmor frequencies ν_0 were 122.41 and 194.37 MHz at room temperature for ^{93}Nb and ^{7}Li, respectively. A spectral analysis was carried out using Bruker MAS probe with a cylindrical 2.5 mm o.d. zirconia rotor at a spinning frequency of 25 kHz. NMR spectra were obtained by applying a single pulse sequence and a recycle delay (D_1) of 3 s to guarantee quantitative spectra. The resulting integrated intensities were normalized with respect to the number of counts, mass of the sample, and receiver gain. Transmission electron microscopy (TEM) was performed with an aberration-corrected S/TEM Themis Z G3 (Thermo Fisher Scientific) microscope. Powder samples dispersed in ethanol were spread on holey carbon-coated Cu grids. High-angle annular dark-field (HAADF) STEM images of the pristine sample were recorded at 300 kV, with 21.4 mrad convergence angle and 65−200 mrad collection angles. A Super-X system (four energy-dispersive X-ray detectors) was used to obtain atomic-scale elemental maps. Due to the degradation of the substituted sample under the beam at 300 kV, attempts were made to obtain TEM results at 80 kV.

2.3. Electrochemical Measurements. Free-standing electrodes (WE) containing 75% wt active material, 15% wt conducting agent (Carbon Black by Superior Graphite, Chicago, IL, United States), and 10% wt binder (poly(1,1,2,2-tetrafluoroethylene)—PTFE in H_2O, Sigma-Aldrich) were fabricated via cold rolling by using few drops of ethanol as solvent. Electrode mass loadings ranged from 5 to 8 mg cm^{-2}. 1 M $LiPF_6$ dissolved in 1:1% wt EC/DMC (Solvionic, France, battery grade) was selected as the electrolyte. Two terminal Swagelok cells were used to study the electrochemical behavior of $K_{1-3x}La_x\square_{2x}NbO_3$ electrodes in WE/electrolyte soaked in separator/Li metal configuration. A GF/D Whatman glass fiber membrane of 10 mm diameter was used as the separator. Electrochemical studies were performed using VMP-3 and MPG-200 potentiostats (Biologic

https://doi.org/10.1021/acs.chemmater.4c02869
Chem. Mater. 2025, 37, 3100−3112

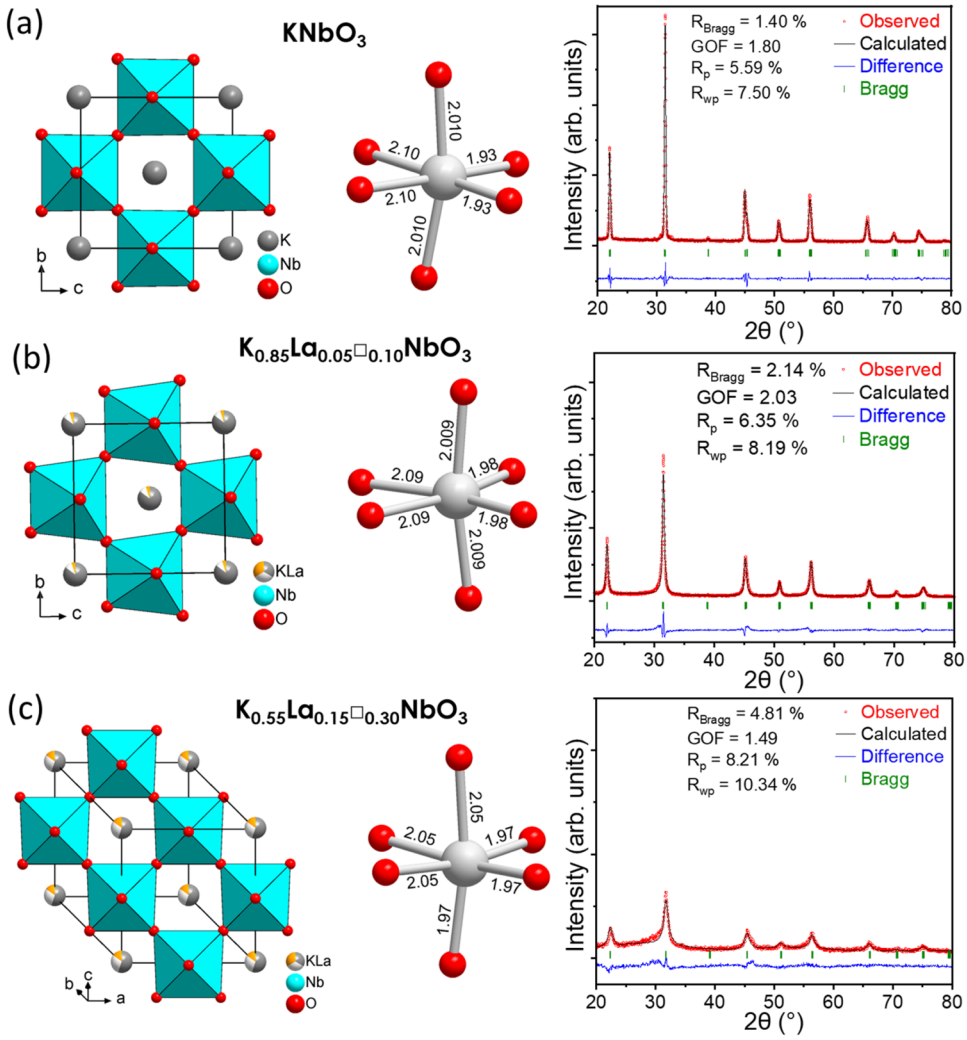

Figure 1. Crystal structure illustration and Rietveld refinement results of powder XRD patterns with experimental, calculated, and difference of (a) pristine $KNbO_3$, (b) $K_{0.85}La_{0.05}\square_{0.10}NbO_3$, and (c) $K_{0.55}La_{0.15}\square_{0.30}NbO_3$ materials. Bond lengths in the [NbO6] octahedra are given in angstroms (Å). Bond valence sums derived from these bond lengths yield values of 4.70(15), 4.50(17), and 4.6(4) for the Nb1 site, respectively.

with ECLab software). Cell assembly and postmortem experiments were conducted in an argon-filled glovebox (O_2 and H_2O < 1 ppm). Cyclic voltammetry (CV) was initially performed for all samples at different scan rates of 0.1, 0.2, 0.5, 1, 2, 5, 10, 20, 30, and 50 mV s^{-1} in 1.2−3.0 V potential window vs. Li^+/Li. Afterward, keeping a fixed scan rate of 10 mV s^{-1}, a lower cutoff potential was systematically investigated. For Li^+ storage performance, galvanostatic charge−discharge (GCPL) measurements were performed in a two-electrode Swagelok cell under 0.05−3.0 V potential window vs. Li^+/Li at current densities of 0.02, 0.05, 0.1, 0.2, 0.5, 1.0, 2.0, and 3.0 A g^{-1}. Cyclic stability tests were carried out at a current density of 0.1 A g^{-1}. CV measurements were conducted to analyze the storage mechanism and kinetics, while GCPL measurements were used to evaluate the Li^+ storage performance of the material. *In situ* XRD measurements were performed at a low current density of 0.01 A g^{-1} with a 1-h pattern acquisition and relaxation time, and under 0.05−3.0 V potential window vs. Li^+/Li. For *ex situ* NMR measurements, electrodes were cycled at different cutoff potentials vs Li^+/Li using cyclic voltammetry at a low scan rate of 0.1 mV s^{-1}. An open circuit potential step (OCP) of 40 h was performed at each cutoff. For *ex situ* analysis, cells were disassembled in a glovebox and electrodes were washed in DMC solution.

3. RESULTS AND DISCUSSION

3.1. Crystal Structure and Physical Characterizations.

XRD analysis of $KNbO_3$, $K_{0.85}La_{0.05}\square_{0.10}NbO_3$, and $K_{0.55}La_{0.15}\square_{0.30}NbO_3$ powders was performed to investigate the changes in the crystal structure upon substitution. All of the samples exhibited a single phase with no discernible impurity phases. Rietveld refinements confirmed the orthorhombic structure of $KNbO_3$ (*Amm*2 space group) as reported previously.[26,27] The refinements using a higher symmetry space group (*R*3*m*) were performed as well; however, they did not give a good agreement, validating the use of the orthorhombic space group. As La^{3+} has an ionic radius of 1.36 Å for the given coordination, it can effectively substitute K^+ with an ionic radius of 1.64 Å at the A-site. Therefore, partial substitution according to the general formula $K_{1-3x}La_x\square_{2x}NbO_3$ was systematically introduced into the structure until the appearance of any secondary phase. The reaction for K^+ to La^{3+} substitution is described by eq 1

$$La_2O_3 \rightarrow 2La_K^{\bullet\bullet} + 3O_o^x + 4V_K' \quad (1)$$

Considering charge neutrality, the effect of substitution at the same Wyckoff position is compensated by generating

https://doi.org/10.1021/acs.chemmater.4c02869
Chem. Mater. 2025, 37, 3100−3112

Table 1. Crystal Structure, Lattice Parameters, and Crystallite Size Details of K_{1-3x} La_x $\square_{2x}$ NbO_3 for $0 \leq x \leq 0.15$ Samples Obtained by Rietveld Refinements

formula	space group	a (Å)	b (Å)	c (Å)	V (Å^3)	crystallite size (nm)
$KNbO_3$	*Amm*2	3.99562(16)	5.6870(4)	5.6999(4)	129.520(14)	125(2)
$K_{0.85}La_{0.05}\square_{0.10}NbO_3$	*Amm*2	4.0011(5)	5.6716(11)	5.6878(11)	129.07(4)	26(1)
$K_{0.55}La_{0.15}\square_{0.30}NbO_3$	*R*3*m*	5.670(7)		6.930(18)	192.9(6)	10(1)

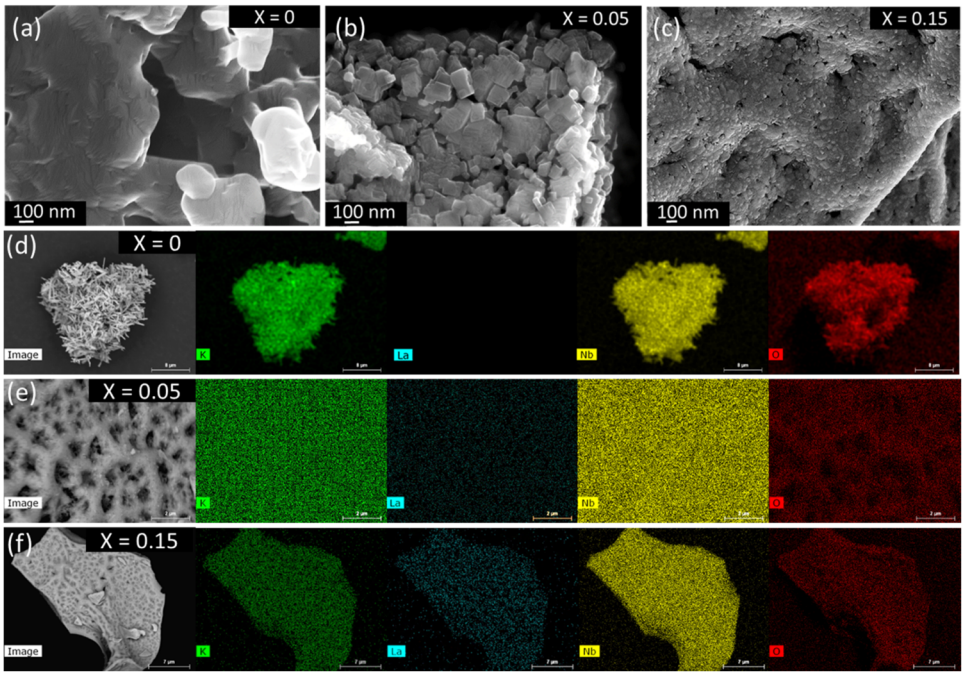

Figure 2. Effect of La substitution on the morphology of materials. SEM images of (a) $KNbO_3$ (pristine); (b) $K_{0.85}La_{0.05}\square_{0.10}NbO_3$ (5% La substitution); and (c) $K_{0.55}$ $La_{0.15}\square_{0.30}NbO_3$ (15% La substitution). EDX mapping showing a uniform distribution of elements in (d) $KNbO_3$ (pristine); (e) $K_{0.85}La_{0.05}\square_{0.10}NbO_3$ (5% La substitution); and (f) $K_{0.55}La_{0.15}\square_{0.30}NbO_3$ (15% La substitution).

cationic vacancies, without altering the anion concentration. The diffractograms of $KNbO_3$, $K_{0.85}La_{0.05}\square_{0.10}NbO_3$, and $K_{0.55}La_{0.15}\square_{0.30}NbO_3$ indicate the phase-pure synthesis of materials with a successful La substitution up to x = 0.15. The Goldschmidt tolerance factor (t) calculated for $KNbO_3$ was 1.06. Such value suggests the formation of a stable perovskite structure.[28,29] However, due to vacancies in the La-substituted structures, the t values decreased to 0.99 and 0.87 for x = 0.05 and 0.15, respectively. Considering the smaller ionic radius of La^{3+} compared to K^+ as well as the presence of vacancies, these values still correspond to a perovskite structure. These values may correspond to a perovskite structure with reduced stability of perovskite cage. This was confirmed in case of materials synthesized with La substitutions above 15%, where the perovskite structure was eventually disturbed and for which a secondary phase of $K_2Nb_6O_{17}$ was detected (Figure S2a).

Rietveld refinements analysis showed that by increasing La substitution, the structure transforms to a more symmetrical space group (from *Amm*2 to *R*3*m* in case of higher substitution), as shown in Figure 1a–c. This is mainly due to a reduced $[NbO]_6$ octahedra distortion, which stabilizes the local structure by increasing configuration entropy.[30,31] With La substitution at A-site, the reflections of diffraction patterns systematically transformed to a broader full width at half-maxima and lower intensities, indicating a stress caused by substitution of La atom in the lattice, which limits the grain growth. This difference implies that there is a trend of reduced crystallite size concomitant with La substitution, which is in agreement with SEM observations. An ∼90% reduction of crystallite size is obtained for 15% La substitution compared to pristine material (from 125 to 10 nm), which is a significant change unlike what is commonly reported in the literature.[23,25] The $K_{1-3x}La_x\square_{2x}NbO_3$ system inhibits more disorder due to a cumulative effect of La substitution and cationic vacancies. This can be possibly explained in two ways: (i) partially replacing K^+ with La^{3+} creates a mismatch in ionic radii; as a result, the structure attempts to accommodate the size difference, which causes local distortions in the lattice due to substitution-induced strain effect; and (ii) the creation of cation vacancies disrupts the long-range order, increasing the number of grain boundaries within the material. Furthermore, the artificial vacancies and La substitution might not be uniformly distributed, leading to regions with varying degrees of strains and defects. This inhomogeneous strain distribution contributes to the observed peak asymmetry in substituted compounds. The details of space group, lattice parameters, cell volume, and crystallite sizes of all the samples obtained through refinements are presented in Table 1.

According to Figure S2b, the (101) and (200) main peaks position shifted toward higher 2θ, which represent a contraction of unit cell volume upon La substitution. This decrease in cell volume is consistent with the replacement of K^+ ions by La^{3+} ions, which have a smaller ionic radius.[32] Specifically, the cell volumes for the structures with x = 0, 0.05, and 0.15 are 129.52, 129.07, and 128.6 Å^3 (calculated as 192.9

https://doi.org/10.1021/acs.chemmater.4c02869
Chem. Mater. 2025, 37, 3100−3112

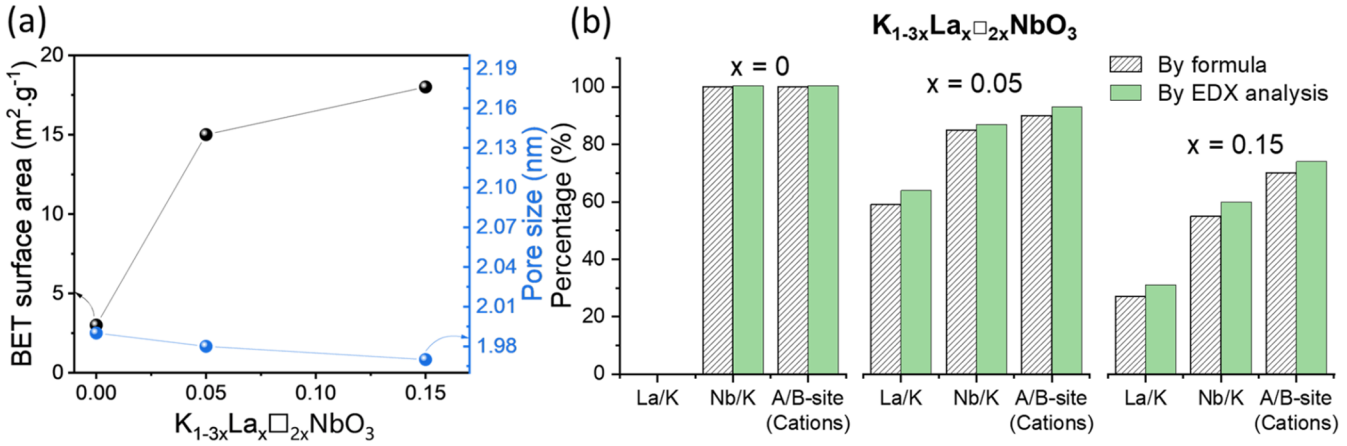

Figure 3. $K_{1-3x}La_x\square_{2x}NbO_3$ (x = 0, 0.01, 0.15) materials with (a) elemental contribution obtained by EDX and comparison with the corresponding theoretical values. The A-site/B-site confirms the presence of vacancies in the substituted structures. (b) Effect of La substitution on BET surface area and pore size.

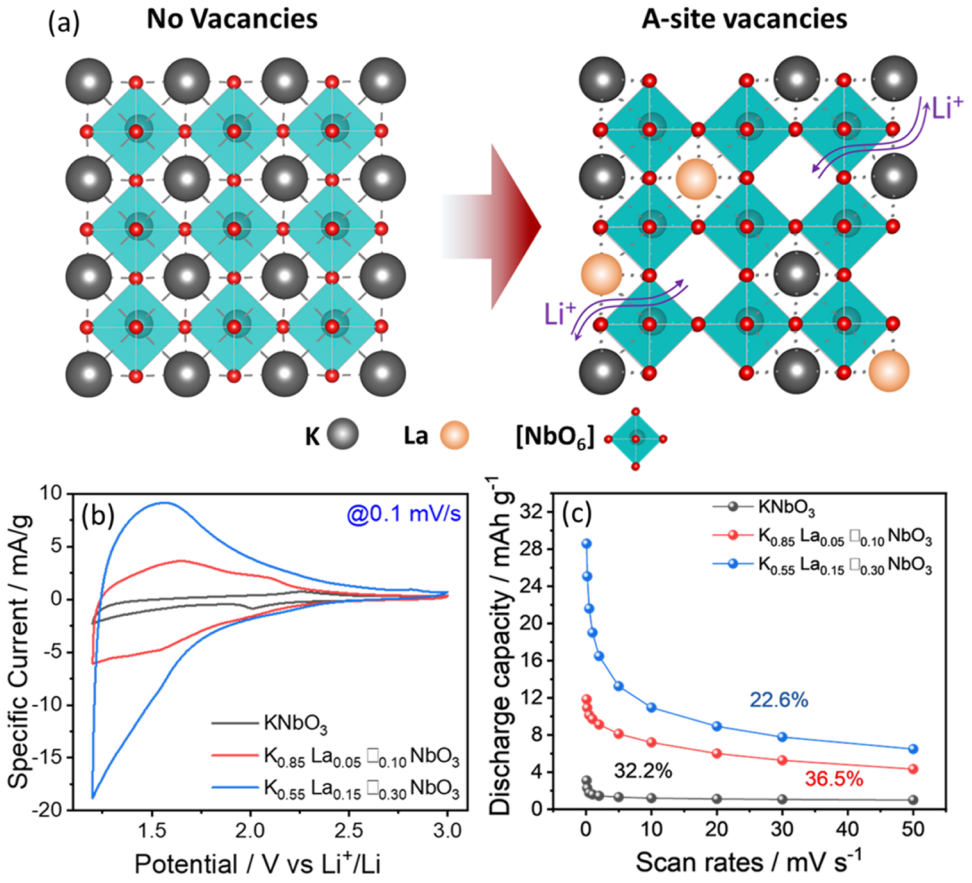

Figure 4. $K_{1-3x}La_x\square_{2x}NbO_3$ (x = 0, 0.05, 0.15) materials with (a) structural representation, where A-site vacancies act as Li^+ insertion sites. (b) Cyclic voltammograms at 0.1 mV s^{-1} in the potential window 1.2−3.0 V vs Li. (c) Comparison of capacity retention at different scan rates under 1.2−3.0 V potential window vs Li.

$Å^3 \times 2/3$ for x = 0.15), respectively. The aliovalent substitution of K^+ by La^{3+} leads either to the formation of cationic vacancies in the A-site, or to the introduction of interstitial oxygen sites, although the latter is structurally unlikely to happen in our case. Further details of the adopted refinement model and obtained results are presented in Table S1 in Supporting Information.

La substitution affects the morphology of the material as observed by SEM analysis. Figure 2a shows the $KNbO_3$ pristine material with lamellar textured rod-shaped particles, which are necked together and agglomerated. Materials synthesized by the sol−gel route typically exhibit agglomeration of smaller individual particles. With 5% of La substitution, the lamellar morphology becomes more pronounced into well-connected and stacked platelets (Figure 2b). However, at 15% La substitutions, the particles grow into a spherical-shaped uniform morphology (Figure 2c). Further, the morphology evolution with increasing La substitution is

https://doi.org/10.1021/acs.chemmater.4c02869
Chem. Mater. 2025, 37, 3100−3112

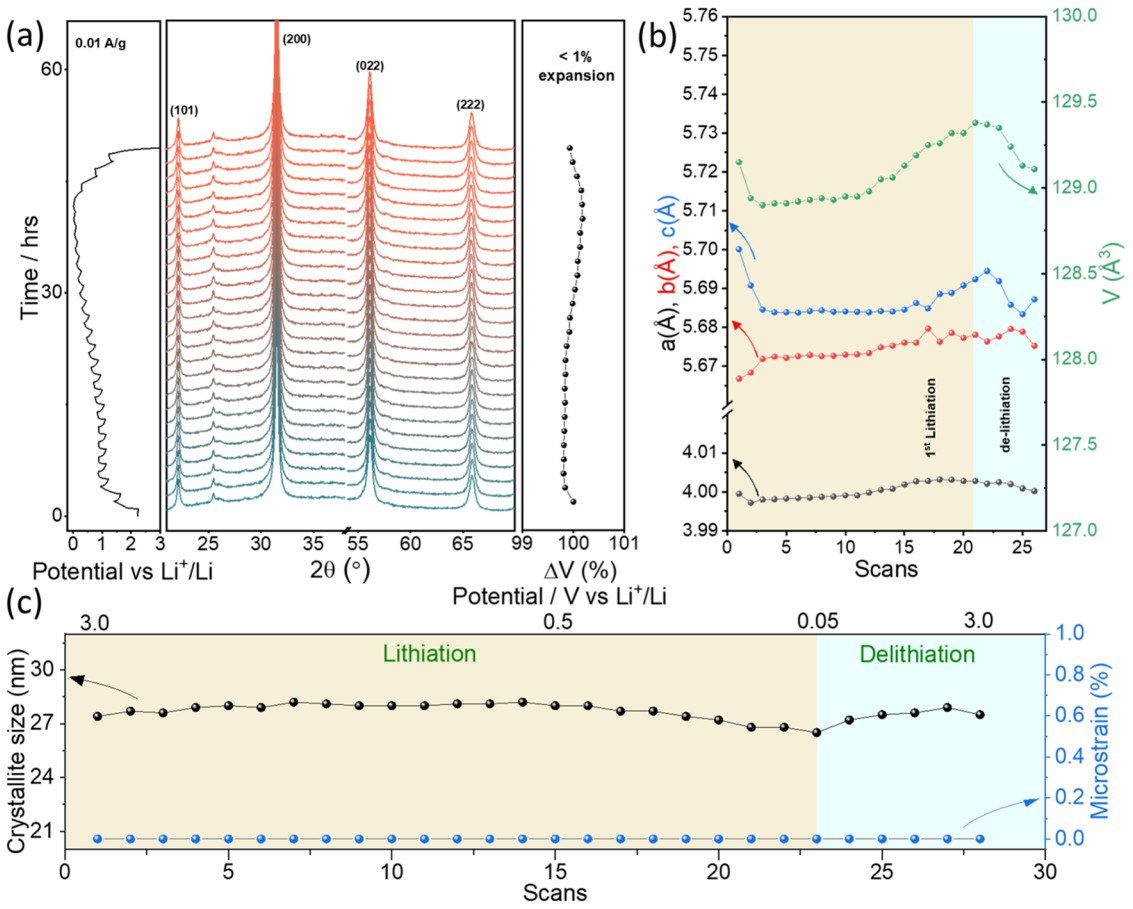

Figure 5. In situ XRD characterizations of the $K_{0.85}La_{0.05}\square_{0.10}NbO_3$ sample at 0.01 A·g^{-1} (a) XRD patterns with corresponding potential-time curve and percentage volume variations upon the 1st cycle. (b) Rietveld refinement results showing lattice parameters and cell volume evolution. (c) Crystallite size and microstrain evolution upon 1st cycle lithiation−delithiation. No change in microstrains indicate "zero-strain" characteristics of $K_{0.85}La_{0.05}\square_{0.10}NbO_3$ material.

shown in Figure S3a−d. These results show a decrease in particle size by increasing the La concentration, which is in agreement with the XRD analysis. In addition, the EDX mapping in Figure 2d−f indicates the homogeneous distribution of cations in the materials.

To visualize the vacancies and their ordering in the structures, HAADF-STEM observations were attempted. Figure S4a shows the HAADF-STEM image of $KNbO_3$ at low magnification, which clearly evidences the absence of any defects or impurity in the material. In the high-resolution image, a well-defined atomic periodicity can be seen (Figure S4b). In Figure S4c, the corresponding EDX map exhibits a uniform distribution of K and Nb atoms, in agreement with the crystal structure of a perovskite oxide. Individual EDX elemental distributions for K, Nb, and O are also shown in Figure S4d−f. Unfortunately, we were unsuccessful in obtaining such atomic maps for substituted samples because of a phase change in materials under the electron beam (see Figure S5).

Due to decrease in particle size, the specific surface area of substituted materials increases, a characteristic confirmed by nitrogen adsorption BET measurements. As shown in Figure 3a, the surface area values obtained are 3, 15, and 18 m^2·g^{-1} for $KNbO_3$, $K_{0.85}La_{0.05}\square_{0.10}NbO_3$, and $K_{0.55}La_{0.15}\square_{0.30}NbO_3$, respectively. In addition, these materials exhibit mesoporosity with an average pore size of 2 nm and La substitution has no significant effect on this value. The EDX elemental analysis of K, La, and Nb presented as a bar chart in Figure 3b confirms the target composition in agreement with the proposed chemical formula. The A- to B-site cation ratios indicate the presence of vacancies in the substituted materials.

3.2. Li$^+$ Storage Behavior of $K_{1-3x}La_x\square_{2x}NbO_3$ Materials. The electrochemical measurements of $K_{1-3x}La_x\square_{2x}NbO_3$ materials at x = 0, 0.05, and 0,15 were performed to investigate the ability of the related structures to reversibly intercalate Li$^+$ cations. Cyclic voltammetry (CV) at a low scan rate of 0.1 mV·s^{-1} (which corresponds to 5 h of charge) within a potential window of 1.2−3.0 V vs Li$^+$/Li was initially chosen based on the electrochemical stability window of typical Nb-based oxide materials reported in literature.[33] As shown in Figure 4a, the pristine $KNbO_3$ structure is closely packed and has no open channels, whereas in the case of La-substituted materials, vacancies exist and, concomitantly, Li$^+$ insertion can be expected. According to the results depicted in Figure 4b, $KNbO_3$ only exhibits negligible electrochemical activity, which corresponds to a specific capacity of 3 mAh·g^{-1}. The substituted materials at x = 0.05 and 0.15 show electrochemical activity with enhanced specific current, giving a specific capacity of 12 and 30 mAh·g^{-1}, respectively. This indicates that the specific capacity increases with the amount of A-site vacancies in the perovskite structure.

Based on one lithium insertion per vacancy, the calculated theoretical capacities are 0, 15, and 43 mAh·g^{-1} for $KNbO_3$, $K_{0.85}La_{0.05}\square_{0.10}NbO_3$, and $K_{0.55}La_{0.15}\square_{0.30}NbO_3$, respectively,

https://doi.org/10.1021/acs.chemmater.4c02869
Chem. Mater. 2025, 37, 3100−3112

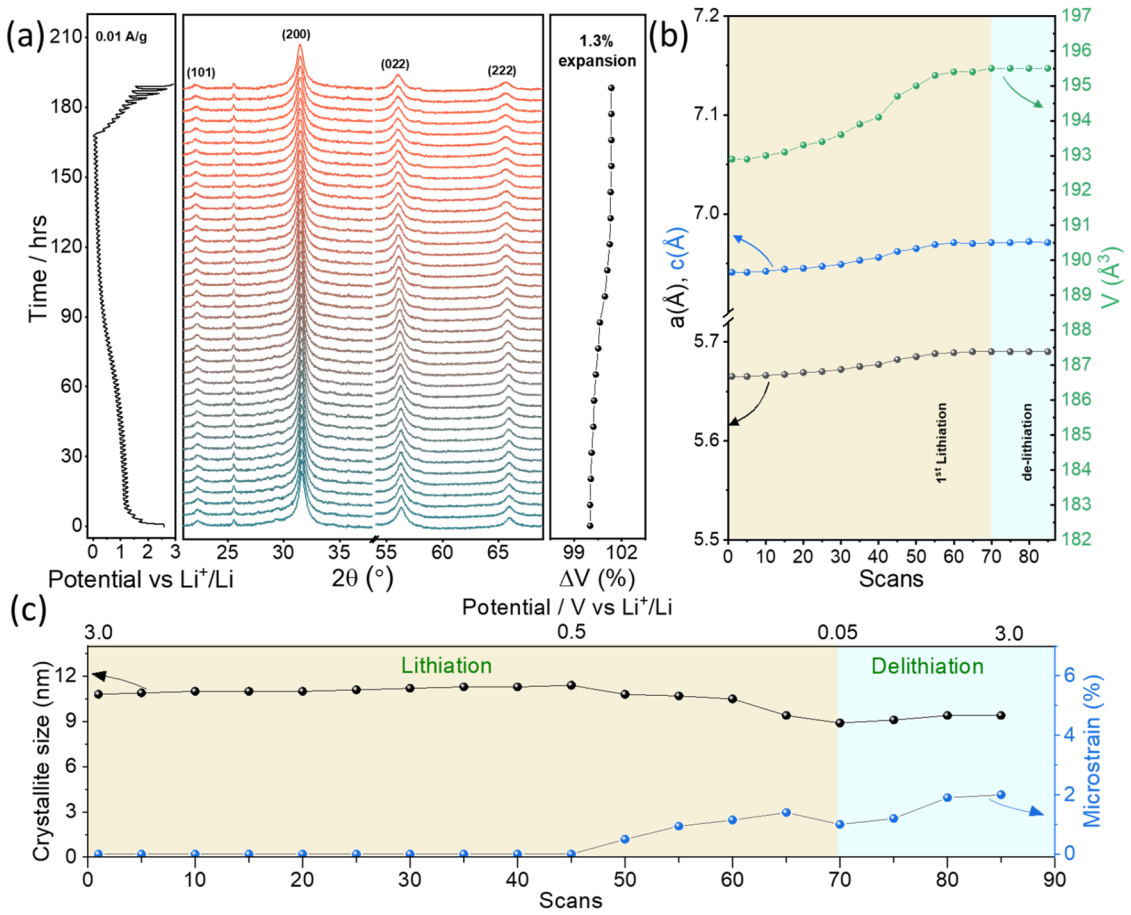

Figure 6. In situ XRD characterizations of the $K_{0.55}La_{0.15}\square_{0.30}NbO_3$ sample at 0.01 A·g^{-1}. (a) XRD patterns with the corresponding potential-time curve and percentage volume variations upon the 1st cycle. (b) Rietveld refinement results showing lattice parameter and cell volume evolution. (c) Crystallite size and microstrain evolution upon 1st cycle lithiation−delithiation.

which are comparable with the experimental values except for $K_{0.55}La_{0.15}\square_{0.30}NbO_3$. The discrepancy observed for this latter compound can be attributed to the significantly reduced crystallinity and shrinkage of the unit cell due to higher La substitution, which also affects vacancy concentration. Consequently, the consideration of one Li^+ insertion/vacancy is compromised. Li^+ insertion in the substituted structures can be considered by following reaction (eq 2)

$$K_{1-3x}La_{2x}\square_{2x}NbO_3 + yLi^+ + ye^- \rightarrow Li_yK_{1-3x}La_{2x}\square_{2x}NbO_3 \quad (2)$$

With increasing sweep rate, the specific capacity decreases as shown in Figure 4c. At 2 mV.s^{-1} (15 min of oxidation or reduction scan), materials retained specific capacity with 50, 75, and 55% retention for $KNbO_3$, $K_{0.85}La_{0.05}\square_{0.10}NbO_3$, and $K_{0.55}La_{0.15}\square_{0.30}NbO_3$, respectively. CVs at different scan rates for all of the samples are compared in Figure S6. In addition, at an extremely high scan rate of 50 mV.s^{-1} (36 s of charge), a capacity retention of 32, 36, and 23% was obtained for $KNbO_3$, $K_{0.85}La_{0.05}\square_{0.10}NbO_3$, and $K_{0.55}La_{0.15}\square_{0.30}NbO_3$, respectively. Despite low capacity values, these compounds are still able to intercalate Li^+ even at very fast scan rates.

To gain further insights about Li^+ storage behavior, the electrochemical stability of these structures was investigated under extended potential windows vs Li^+/Li. Interestingly, the materials withstand well for reducing potentials up to 10 mV vs Li. Although the CV shapes are well recovered after reaching lower cutoff potentials without significant electrochemical activity loss for pristine $KNbO_3$, a slight reduction in electrochemical activity was observed for the highly substituted $K_{0.55}La_{0.15}\square_{0.30}NbO_3$, as shown in Figure S7. This implies that the substituted structures may undergo structural changes. This hypothesis has been investigated through *in situ* XRD analysis, which is provided in the next section.

3.3. Crystal Structure Evolution during Charge/Discharge. *In situ* XRD analysis was performed to better understand the structural changes upon lithium (de) insertion into the different structures in order to elucidate the underlying lithiation mechanism. Following the electrochemistry, two substituted samples ($K_{0.85}La_{0.05}\square_{0.10}NbO_3$ and $K_{0.55}La_{0.15}\square_{0.30}NbO_3$) were initially investigated in galvanostatic conditions at 0.01 A·g^{-1} under an extended potential window (0.05−3.0 V vs Li). To better visualize the patterns, the peaks associated with beryllium window were removed from the XRD patterns. The results in Figure 5a show that (i) existing peaks do not disappear and no new peaks appear during the lithiation and delithiation processes, indicating that $K_{0.85}La_{0.05}\square_{0.10}NbO_3$ follows a solid-solution mechanism as previously reported for other compounds in the literature,[34,35] and (ii) the structure exhibits no prominent peak shift for the (101), (200), (022), and (222) peaks, which implies that lattice parameters are not significantly affected during Li^+ insertion into vacancies. These characteristics

https://doi.org/10.1021/acs.chemmater.4c02869
Chem. Mater. 2025, 37, 3100−3112

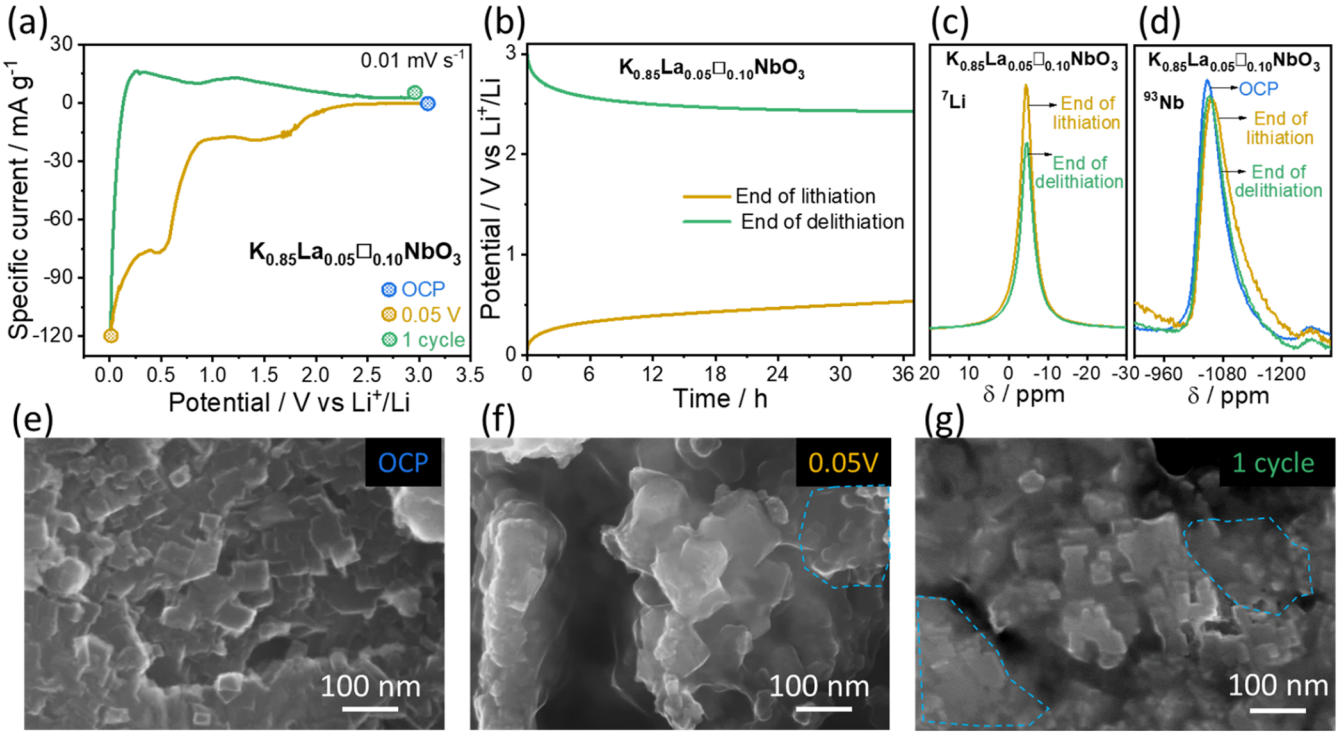

Figure 7. 1st cycle postmortem diagnosis of $K_{0.85}La_{0.05}\square_{0.10}NbO_3$ through ex situ NMR and ex situ SEM. (a) Cyclic voltammetry of three cells cycled at different cutoff potentials: OCP, 0.05 V, and 1 complete cycle, respectively. (b) Self-discharge curves after cutoff at 0.05 V and 1 cycle. (c) ^{7}Li MAS NMR at 0.05 V and 1 cycle cutoff. (d) ^{93}Nb MAS NMR at OCV, 0.05 V, and 1 cycle cutoff. Ex situ SEM at (e) OCP, (f) 0.05 V cutoff, and (g) after 1 complete cycle. The blue dotted area represents the SEI coverage on the particles.

confirm the "zero-strain" nature of the $K_{0.85}La_{0.05}\square_{0.10}NbO_3$ material, similar to the A-site vacant structures reported by Le Calvez et al.[16] However, upon further investigation, a slight reduction in diffraction peak intensities with a minor shift in peak positions was observed during lithiation. While it was difficult to accurately determine and compare the peak shifts along the preferred direction due to minimal shift, Rietveld refinements were performed to obtain deeper insights.

The refinements were successful and results at OCP were in agreement with the pristine powder samples, which indicate that the electrode preparation process did not affect the structural integrity of the materials. $K_{0.85}La_{0.05}\square_{0.10}NbO_3$ shows a slight increase in lattice parameters, indicating a volume expansion upon lithiation. However, the variations are quite small, with "*c*" parameter changing slightly more, as can be seen from Figure 5b. At the end of lithiation, a maximum volume expansion of less than 1% was obtained. During delithiation, almost a complete reversibility of lattice parameters toward the original state was achieved. In addition, the lithiation−delithiation process causes a reversible change in apparent particle size without inducing any macrostrains (Figure 5c). This confirms that vacancies play a crucial role in balancing local strains, thereby enabling the material to achieve a "zero-strain" characteristic. Such a behavior suggests that the structure remains intact upon reversible Li^+ insertion, which has significant effects on electrochemical performance, particularly cyclic stability.

The *in situ* XRD performed for $K_{0.55}La_{0.15}\square_{0.30}NbO_3$ and the patterns are depicted in Figure 6a. It follows a structural evolution during (de) lithiation similar to $K_{0.85}La_{0.05}\square_{0.10}NbO_3$, however with more pronounced effects. At the end of lithiation, a noticeable peak shift is observed on the patterns unlike $K_{0.85}La_{0.05}\square_{0.10}NbO_3$, confirming an increased lithium insertion due to higher concentration of A-site vacancies (30%) in $K_{0.55}La_{0.15}\square_{0.30}NbO_3$. The refinement results in Figure 6b show the variations in cell parameters during a complete lithiation−delithiation cycle. It can be noted that no preferential Li^+ insertion occurs as both "*a*" and "*c*" parameters evolve equally. It means that vacancies are distributed in a disordered fashion providing random pathways for Li^+ transport into the bulk of the electrode material. Interestingly, the volume expansion was still small, with ∼1.3% value obtained at the end of lithiation. However, the cell parameters and volume variations were irreversible upon delithiation, an effect that was less prominent in case of $K_{0.85}La_{0.05}\square_{0.10}NbO_3$. Additionally, Figure 6c shows that the local microstrains started to appear after 0.5 V during the first lithiation (a region with relatively enhanced ΔV), which were irreversible upon delithiation. One possible explanation can be that the Li^+ extraction from the structure upon delithiation is incomplete and some lithium is irreversibly trapped in the structure during first cycle. Second, the crystallite size of the material decreases, while cell volume and microstrain increases. This indicates that the particles undergo an irreversible and partial extrusion during lithiation, which helped to compensate the stresses induced by formation of the lithiated phase $Li_xK_{0.55}La_{0.15}\square_{0.30}NbO_3$. This effect has been reported in certain transition metal oxides,[36,37] where electrochemically induced partial amorphization enhances Li^+ storage performance. Nevertheless, since the global crystallinity of the material was preserved even under extreme reducing conditions (50 mV vs Li^+/Li), the structure is expected to exhibit superior electrochemical cyclic stability. As a baseline, *in situ* XRD of pristine $KNbO_3$ was performed, and the results are presented

https://doi.org/10.1021/acs.chemmater.4c02869
Chem. Mater. 2025, 37, 3100−3112

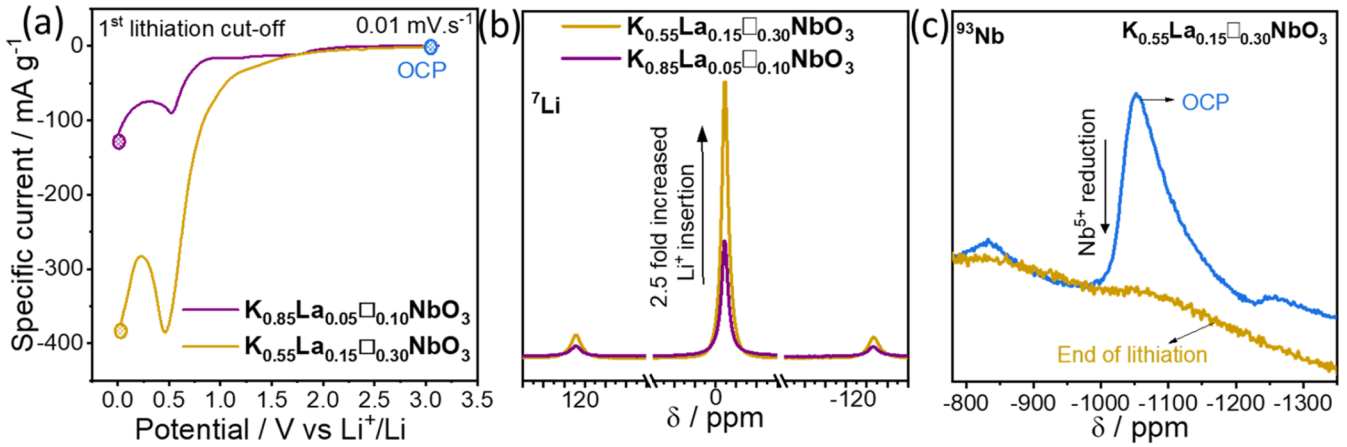

Figure 8. Ex situ NMR comparison for $K_{0.85}La_{0.05}\square_{0.10}NbO_3$ and $K_{0.55}La_{0.15}\square_{0.30}NbO_3$ at the end of lithiation (0.05 V cutoff). (a) Cyclic voltammetry of $K_{0.85}La_{0.05}\square_{0.10}NbO_3$ and $K_{0.55}La_{0.15}\square_{0.30}NbO_3$ at 0.05 V. (b) ^{7}Li MAS NMR comparison of $K_{0.85}La_{0.05}\square_{0.10}NbO_3$ and $K_{0.55}La_{0.15}\square_{0.30}NbO_3$ at 0.05 V. (c) ^{93}Nb MAS NMR at OCP and 0.05 V for $K_{0.55}La_{0.15}\square_{0.30}NbO_3$.

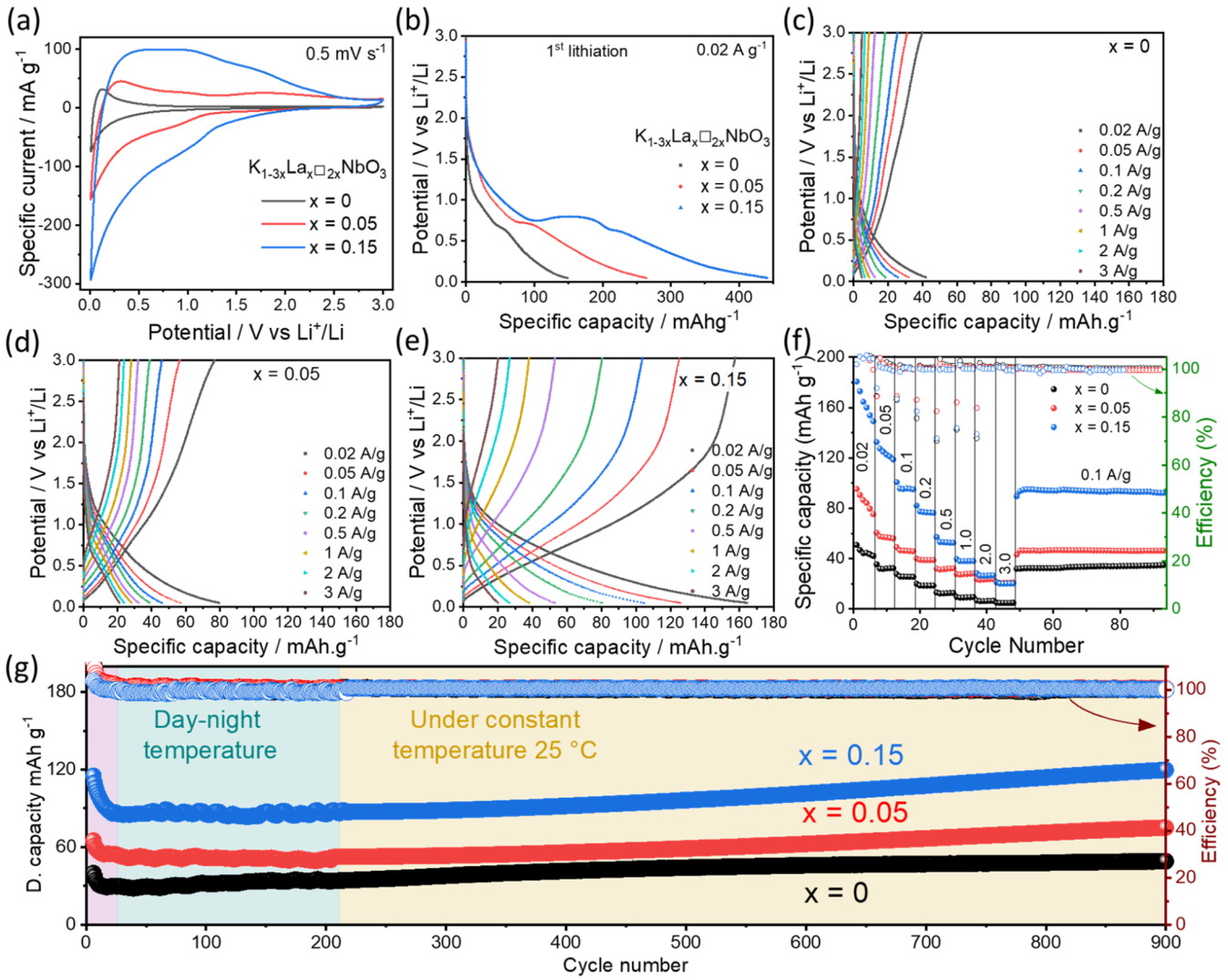

Figure 9. Li^+ storage performance of $K_{1-3x}La_x\square_{2x}NbO_3$ (x = 0, 0.05, 0.15) materials under extended potential windows vs Li in half cell configurations. (a) CV comparison at 0.5 mV s^{-1}. (b) 1st lithiation curve of GCPL measurements at 0.02 A·g^{-1}. GCPL curves at different current densities for (c) pristine $KNbO_3$ electrode. (d) $K_{0.85}La_{0.05}\square_{0.10}NbO_3$ electrode. (e) $K_{0.55}La_{0.15}\square_{0.30}NbO_3$ electrode. (f) Overall performance comparison of all of the samples. (g) Cyclic stability for 900 cycles at 0.1 A g^{-1}.

https://doi.org/10.1021/acs.chemmater.4c02869
Chem. Mater. 2025, 37, 3100−3112

in Figure S8. It shows that the structural integrity is intrinsic to pristine material and well preserved in substituted material.

Li^+ insertion into the structure and changes in the Nb local environment are further supported by ^7Li and ^{93}Nb MAS NMR performed in *ex situ* mode. Solid-state NMR spectroscopy has been used as a powerful tool, which provides insights into the electrochemical processes in battery materials.[38−40] Figure 7a corresponds to the cyclic voltammetry of $K_{0.85}La_{0.05}\square_{0.10}NbO_3$ electrodes whose cycling has been stopped at OCP (before any cycling), the end of lithiation (0.05 V vs Li^+/Li), and the end of delithiation (3.0 V vs Li^+/Li) after one complete cycle. A low scan rate of 0.1 mV s^{-1} was selected to ensure complete Li^+ insertion/extraction into the structure and the electrodes were subsequently polarized to allow thermodynamic equilibrium. After 36 h under OCP conditions, the cells showed variations in potentials as they reached equilibrium. Specifically, the electrode at the 0.05 V cutoff potential stabilized at 0.5 V vs Li^+/Li, while the electrode at the 3.0 V cutoff stabilized at 2.5 V vs Li^+/Li, as illustrated in Figure 7b.The ^7Li MAS NMR results depicted in Figure 7c show the appearance of a sharp NMR resonance signal at −5 ppm for the sample recovered at 0.05 V cutoff potential, indicating the presence of Li^+ in the structure. The peak intensity, normalized to the mass and number of scans, is directly proportional to the amount of Li^+ inserted. Upon delithiation to 3.0 V cutoff potential, a slight decrease in intensity occurs, indicating that only a partial extraction of Li^+ is observed, validating our hypothesis of Li^+ cations trapping during the first cycle as observed in other compounds.[41] Hence, this justifies the low Coulombic efficiency during the first cycle as a combinatorial effect of incomplete Li^+ extraction. At the same time, the main peak in the ^{93}Nb MAS NMR spectrum slightly broadened with a reduced intensity at 0.05 V cutoff potential (Figure 7d). Due to partial Li^+ insertion, some Nb^{5+} (diamagnetic, electronic configuration in d^0) are reduced, probably to Nb^{4+}, which are paramagnetic and display one localized electron. Due to the significant electron−nucleus dipolar interaction between the Nb nucleus and the unpaired localized electron at the same site, Nb^{4+} are typically unobservable by ^{93}Nb NMR. Therefore, only the remaining Nb^{5+} can still be detected. This explains the slightly reduced intensity in the ^{93}Nb MAS NMR spectrum. In addition, the formation of some Nb^{4+} will introduce structural distortions in Li and Nb local environments, causing a peak broadening. It is accompanied by a slight apparent shift in peak position (−1047 to −1054 δ/ppm), which is not completely reversible upon delithiation and may be assigned to the local distortions due to trapped Li cations in the vicinity of the $[Nb_6]$ octahedron. However, these effects are less prominent and almost reversible upon delithiation at 3.0 V vs Li^+/Li. Nevertheless, these results indicate that most of the Nb remains unreacted, maintaining 5+ oxidation state. Therefore, a moderated specific capacity is expected for $K_{0.85}La_{0.05}\square_{0.10}NbO_3$. Figure 7e−g shows the *ex situ* SEM of electrodes at OCV, 0.05, and 3.0 V cutoff, respectively. Compared to the image at OCV, particles in lithiated and delithiated electrodes are covered with a thin blurry layer, which is prominent in blue dotted regions and can be referred as the solid electrolyte interface (SEI).[42,43] However, the morphology appears to be unaffected. This analysis provides a basis for explaining the Li^+ insertion behavior of $K_{0.55}La_{0.15}\square_{0.30}NbO_3$. Figures 8a and 8b compare the CV curves at 0.05 V cutoff potential and ^7Li MAS NMR spectra of $K_{0.85}La_{0.05}\square_{0.10}NbO_3$ and $K_{0.55}La_{0.15}\square_{0.30}NbO_3$, respectively. ^7Li MAS NMR results reveal a 2.5-fold increase in lithium insertion into the $K_{0.55}La_{0.15}\square_{0.30}NbO_3$ structure upon lithiation, highlighting the role of high vacancy concentration. Simultaneously, ^{93}Nb MAS NMR confirms the significant reduction of Nb from 5+ to lower oxidation states as the resonance peak intensity significantly decreased (Figure 8c). Only a very-low-intensity and broad signal can still be observed, indicating that Nb^{5+} remains in very low concentration.[17] However, direct observation of reduced Nb^{4+} and/or Nb^{3+} as well as the identification of a nominal oxidation state is not realized, as no new peaks are detectable due to the paramagnetic nature of Nb^{4+} (d^1) and Nb^{3+} (d^2), making them invisible to ^{93}Nb NMR in these experimental conditions.

3.4. Li^+ Storage Performance under Extended Potential Window. The Li^+ storage performance of $K_{1-3x}La_x\square_{2x}NbO_3$ (x = 0, 0.05, 0.15) was investigated under an extended potential window (0.05−3.0 V vs Li^+/Li) in two-electrode Swagelok cells. The cyclic voltammetry (CV) comparison at 0.5 mV s^{-1} is presented in Figure 9a, where substituted materials exhibit more pronounced activity than the pristine perovskite compound, as evidenced by an increase in current response and broadening of CV shape. For $K_{0.55}La_{0.15}\square_{0.30}NbO_3$, a pair of broad redox peaks appears around 1.2 V in addition to the much broadened redox peaks at lower potentials vs Li^+/Li, which could be associated with Nb-redox activity.[34,44,45] These redox peaks are less prominent and appear at a lower potential in case of $K_{0.85}La_{0.05}\square_{0.10}NbO_3$ and $KNbO_3$. This indicates that A-site vacancies enhance the Li^+ accessibility to the perovskite cage and concomitantly the vicinity of $[NbO_6]$ octahedra. Nonetheless, the Nb activity is moderate, with redox potentials exhibiting slight shifts. These shifts are likely attributed to the local chemical environment and the disordered distribution of vacancies. Galvanostatic charge−discharge (GCPL) measurements were carried out and a comparison of first lithiation curves is presented in Figure 9b. The plateau at 0.75 V becomes more prominent with La substitution. It indicates slight irreversible changes in electrode materials during the first cycle, as emphasized by the *in situ* XRD analysis. Additionally, the effect might be combined with electrolyte degradation and the formation of a passivation layer (SEI formation) as previously described.[45,46] It can be pointed out that a relatively higher particle extrusion effect in the $K_{0.55}La_{0.15}\square_{0.30}NbO_3$ material during the first cycle caused unstable SEI formation, an effect that persists in subsequent cycles as well. Figure 9c−e show the charge−discharge plots of pristine $KNbO_3$, $K_{0.85}La_{0.05}\square_{0.10}NbO_3$, and $K_{0.55}La_{0.15}\square_{0.30}NbO_3$ materials, respectively. The measurements were recorded at current densities ranging from 0.02 to 3.0 A g^{-1}. Pristine $KNbO_3$ delivers 41 mAh g^{-1} at 0.02 A g^{-1} and 5 mAh g^{-1} at 3 A g^{-1}. Partially substituted $K_{0.85}La_{0.05}\square_{0.10}NbO_3$ delivered 80 mAh g^{-1} at 0.02 A g^{-1} and 21 mAh g^{-1} at 3 A g^{-1}, while the highly substituted $K_{0.55}La_{0.15}\square_{0.30}NbO_3$ exhibited 164 mAh g^{-1} at 0.02 A g^{-1} and 20 mAh g^{-1} at 3 A g^{-1} (charge and discharge in 24s). This indicates that a capacity retention of 12, 26, and 12% for $KNbO_3$, $K_{0.85}La_{0.05}\square_{0.10}NbO_3$, and $K_{0.55}La_{0.15}\square_{0.30}NbO_3$, respectively, at such high current density. The moderate rate performance of $KNbO_3$ could be due to the intrinsic low electronic conductivity of the host structure, as it has been widely known as a semiconducting materials.[28,47] The overall performance comparison is shown in Figure 9f, where an

https://doi.org/10.1021/acs.chemmater.4c02869
Chem. Mater. 2025, 37, 3100−3112

unstable capacity was obtained during the initial cycling as explained previously. The detailed comparison of capacity decay from cycle 2 to 7 is presented in Figure S9. It was observed that the relative capacity decay for all samples was almost the same, indicating that the increase of La in the structure does not have a detrimental effect on the electrochemical stability. Nevertheless, all of the materials showed stable cycling afterward while maintaining a high Coulombic efficiency.

Long-term cycling of all of the materials was investigated through galvanostatic charge−discharge at 0.1 A g^{-1} for 900 cycles. Initially, cycling was started without a constant temperature, which caused a capacity fluctuation and a constant temperature of 25 °C was adopted afterward. The results in Figure 9g depict an initial capacity decay followed by stable cycling up to first 100 cycles. Interestingly, a constant increase in capacity over cycling is observed for all of the three materials, which can be explained by the formation of a stable electrode−electrolyte interphase over the cycles. After 900 cycles, the specific capacities of $KNbO_3$, $K_{0.85}La_{0.05}\square_{0.10}NbO_3$, and $K_{0.55}La_{0.15}\square_{0.30}NbO_3$ were 49, 75, and 119 mAh g^{-1}, respectively. These values indicate an increase of 39, 33, and 27% in specific capacity after 900 cycles considering the stable capacity values after initial decay. The highly substituted $K_{0.55}La_{0.15}\square_{0.30}NbO_3$ was subjected to extended cycling for over 1500 cycles, demonstrating stable capacity and a high Coulombic efficiency (Figure S10). Postmortem analysis of cycled electrodes was performed using *ex situ* SEM. Given that all of the materials exhibited similar trends in cyclic stability, $K_{0.55}La_{0.15}\square_{0.30}NbO_3$ was selected for further investigation due to its high performance. The results in Figure S11a,b show SEM images of cycled electrodes taken immediately under the electron beam and after a few seconds of focused exposure, respectively. The area highlighted by the green circle indicates the beam damage to the encapsulation layer, termed the SEI. The morphology of pristine $K_{0.55}La_{0.15}\square_{0.30}NbO_3$ powder in Figure S11c can be compared with the zoomed-in image of the cycled electrode in Figure S11d, where particles appear after the removal of the thick SEI under the beam. This observation explains the significant irreversible capacity in the first cycle and a capacity decay over subsequent cycles, which thickened the SEI until it became stable. Once stabilized, the material tends to regain capacity over extended cycling.

4. CONCLUSIONS

In our approach, we developed a strategy of creating artificial vacancies on atomic level in the lattice of a structure. The $KNbO_3$ host structure is tailored by partial substitution of K^+ from the A-site with La^{3+}, generating two vacancies per substitution. The materials were successfully synthesized and the effect of substitutions on the structure was accurately investigated. An increase in lattice symmetry was obtained with La substitutions on the K^+-occupied A-site of the perovskite structure, which results in transformation of the space group from *Amm*2 of pristine $KNbO_3$ to *R*3*m* for $K_{0.55}La_{0.15}\square_{0.30}NbO_3$. Electrochemical measurements confirmed an increase in performance of substituted material for Li^+ storage with 3-fold improvement of the specific capacity and better rate capability compared to pristine structure. Artificial vacancies in the structure acted as Li^+ insertion sites that facilitated Li^+ accessibility to the perovskite cage and concomitantly the vicinity of $[NbO_6]$ octahedra. The structures exhibited enhanced electrochemical stability, as evidenced by a 50 mV vs Li^+/Li cutoff potential, a feature uncommon in Nb-based oxides. *In situ* XRD revealed a solid-solution mechanism with Li^+ migration in the structure without causing significant lattice disturbance. We chose a host structure with relatively low-cost cations and, importantly, a cubic perovskite structure class that is not supposedly meant for ion storage. The vacancies in $K_{1-3x}La_x\square_{2x}NbO_3$ (x = 0, 0.05, 0.15) structure helped in enhanced Li^+ insertion and an increase in performance was achieved.

■ ASSOCIATED CONTENT

Supporting Information

The Supporting Information is available free of charge at https://pubs.acs.org/doi/10.1021/acs.chemmater.4c02869.

Synthesis scheme, XRD refinement data, morphology evolution, HAADF-STEM images, TEM and EDX results, in situ XRD, long-term cycling, postmortem analysis (PDF)

■ AUTHOR INFORMATION

Corresponding Author

Thierry Brousse − *Nantes Université, CNRS, Institut des Matériaux de Nantes Jean Rouxel, IMN, F-44000 Nantes, France; Réseau sur le Stockage Electrochimique de l'Energie (RS2E), CNRS FR 3459, 80039 Amiens, France;* orcid.org/0000-0002-1715-0377; Email: Thierry.Brousse@univ-nantes.fr

Authors

Abbas Khan − *Nantes Université, CNRS, Institut des Matériaux de Nantes Jean Rouxel, IMN, F-44000 Nantes, France; Réseau sur le Stockage Electrochimique de l'Energie (RS2E), CNRS FR 3459, 80039 Amiens, France*

Eric Quarez − *Nantes Université, CNRS, Institut des Matériaux de Nantes Jean Rouxel, IMN, F-44000 Nantes, France;* orcid.org/0000-0001-7887-892X

Nicolas Dupré − *Nantes Université, CNRS, Institut des Matériaux de Nantes Jean Rouxel, IMN, F-44000 Nantes, France;* orcid.org/0000-0002-0687-9357

Eric Gautron − *Nantes Université, CNRS, Institut des Matériaux de Nantes Jean Rouxel, IMN, F-44000 Nantes, France*

Andrea Balducci − *Institute of Technical Chemistry and Environmental Chemistry and Center for Energy and Environmental Chemistry, Friedrich-Schiller-University Jena, 07743 Jena, Germany;* orcid.org/0000-0002-2887-8312

Olivier Crosnier − *Nantes Université, CNRS, Institut des Matériaux de Nantes Jean Rouxel, IMN, F-44000 Nantes, France; Réseau sur le Stockage Electrochimique de l'Energie (RS2E), CNRS FR 3459, 80039 Amiens, France*

Complete contact information is available at: https://pubs.acs.org/10.1021/acs.chemmater.4c02869

Notes

The authors declare no competing financial interest.

■ ACKNOWLEDGMENTS

Abbas Khan as a part of the DESTINY PhD programme (Doctorate programme on Emerging battery Storage Technologies INspiring Young scientists) acknowledges funding from the European Union's Horizon 2020 research and innovation programme under the Marie Skłodowska-Curie

Actions Cofund Grant Agreement No: 945357. This work was also performed within the framework of two projects: HIPOHYBAT project funded by the "France 2030" government investment plan managed by the French Research Agency, under the reference ANR-22-PEBA-0003, and Labex STORE-EX (ANR-10-LABX-76-01). The authors also thank Nicolas Stephant for SEM images and Stéphane Grolleau for BET measurements. Measurements were performed using the IMN's characterisation platform, PLASSMAT, Nantes, France.

REFERENCES

(1) Armand, M.; Tarascon, J.-M. Building Better Batteries. *Nature* **2008**, *451* (7179), 652−657.
(2) Liu, Y.; Zhu, Y.; Cui, Y. Challenges and Opportunities towards Fast-Charging Battery Materials. *Nat. Energy* **2019**, *4* (7), 540−550.
(3) Uhlmann, C.; Illig, J.; Ender, M.; Schuster, R.; Ivers-Tiffée, E. In Situ Detection of Lithium Metal Plating on Graphite in Experimental Cells. *J. Power Sources* **2015**, *279*, 428−438.
(4) Choi, C.; Ashby, D. S.; Butts, D. M.; DeBlock, R. H.; Wei, Q.; Lau, J.; Dunn, B. Achieving High Energy Density and High Power Density with Pseudocapacitive Materials. *Nat. Rev. Mater.* **2020**, *5* (1), 5−19.
(5) Ohzuku, T.; Ueda, A.; Yamamoto, N. Zero-Strain Insertion Material of Li [Li1/3Ti5/3] O 4 for Rechargeable Lithium Cells. *J. Electrochem. Soc.* **1995**, *142* (5), 1431−1435.
(6) Prakash, A. S.; Manikandan, P.; Ramesha, K.; Sathiya, M.; Tarascon, J.-M.; Shukla, A. K. Solution-Combustion Synthesized Nanocrystalline $Li_4Ti_5O_{12}$ As High-Rate Performance Li-Ion Battery Anode. *Chem. Mater.* **2010**, *22* (9), 2857−2863.
(7) Lu, X.; Jian, Z.; Fang, Z.; Gu, L.; Hu, Y.-S.; Chen, W.; Wang, Z.; Chen, L. Atomic-Scale Investigation on Lithium Storage Mechanism in $TiNb_2O_7$. *Energy Environ. Sci.* **2011**, *4* (8), 2638.
(8) Griffith, K. J.; Wiaderek, K. M.; Cibin, G.; Marbella, L. E.; Grey, C. P. Niobium Tungsten Oxides for High-Rate Lithium-Ion Energy Storage. *Nature* **2018**, *559* (7715), 556−563.
(9) Saber, M.; Preefer, M. B.; Kolli, S. K.; Zhang, W.; Laurita, G.; Dunn, B.; Seshadri, R.; Van Der Ven, A. Role of Electronic Structure in Li Ordering and Chemical Strain in the Fast Charging Wadsley−Roth Phase PNb_9O_{25}. *Chem. Mater.* **2021**, *33* (19), 7755−7766.
(10) Bashian, N. H.; Zhou, S.; Zuba, M.; Ganose, A. M.; Stiles, J. W.; Ee, A.; Ashby, D. S.; Scanlon, D. O.; Piper, L. F. J.; Dunn, B.; Melot, B. C. Correlated Polyhedral Rotations in the Absence of Polarons during Electrochemical Insertion of Lithium in ReO_3. *ACS Energy Lett.* **2018**, *3* (10), 2513−2519.
(11) Kennedy, B. J.; Howard, C. J.; Kubota, Y.; Kato, K. Phase Transition Behaviour in the A-Site Deficient Perovskite Oxide $La_{1/3}NbO_3$. *J. Solid State Chem.* **2004**, *177* (12), 4552−4556.
(12) Liang, G.; Yang, L.; Xiong, X.; Pei, K.; Zhao, X.; Wang, C.; You, W.; Liu, X.; Zhang, X.; Che, R. Interfacial Space Charge Enhanced Sodium Storage in a Zero-Strain Cerium Niobite Perovskite Anode. *Adv. Funct. Mater.* **2022**, *32* (43), No. 2206129.
(13) Liang, G.; Yang, L.; Xiong, X.; Liu, X.; Zhang, X.; Che, R. High-Rate Electrochemical Lithium-Ion Storage through Li^+ Intercalation Pseudocapacitance in the $Pr_{1/3}NbO_3$ Anode. *J. Mater. Chem. A* **2022**, *10* (44), 23675−23682.
(14) Nakayama, M.; Ikuta, H.; Uchimoto, Y.; Wakihara, M.; Terada, Y.; Miyanaga, T.; Watanabe, I. Changes in Local Structure during Electrochemical Li Insertion into A-Site Deficient Perovskite Oxides, $La_{1/3}NbO_3$. *J. Phys. Chem. B* **2003**, *107* (39), 10715−10721.
(15) Nakayama, M.; Uchimoto, Y.; Wakihara, M. Investigation on Cyclability in $Li_xLa_{1/3}NbO_3$ Electrode Material for Rechargeable Lithium Ion Battery. *J. Power Sources* **2005**, *146* (1−2), 674−677.
(16) Le Calvez, E.; Espinosa-Angeles, J. C.; Whang, G. J.; Dupré, N.; Dunn, B. S.; Crosnier, O.; Brousse, T. Investigating the Perovskite $Ag_{1-3x}La_xNbO_3$ as a High-Rate Negative Electrode for Li-Ion Batteries. *Front. Chem.* **2022**, *10*, No. 873783.
(17) Khan, A.; Orbay, M.; Dupré, N.; Gautron, E.; Calvez, E. L.; Crosnier, O.; Balducci, A.; Brousse, T. Lithium Storage Behaviour of $AgNbO_3$ Perovskite: Understanding Electrochemical Activation and Charge Storage Mechanisms. *Energy Storage Mater.* **2024**, *70*, No. 103431.
(18) Wang, D.; Wang, G.; Lu, Z.; Al-Jlaihawi, Z.; Feteira, A. Crystal Structure, Phase Transitions and Photoferroelectric Properties of $KNbO_3$-Based Lead-Free Ferroelectric Ceramics: A Brief Review. *Front. Mater.* **2020**, *7*, 91.
(19) Waqar, M.; Wu, H.; Chen, J.; Yao, K.; Wang, J. Evolution from Lead-Based to Lead-Free Piezoelectrics: Engineering of Lattices, Domains, Boundaries, and Defects Leading to Giant Response. *Adv. Mater.* **2022**, *34* (25), No. 2106845.
(20) Dubernet, M.; Pitcher, M. J.; Zaghrioui, M.; Bah, M.; Bustillo, J.; Giovannelli, F.; Monot-Laffez, I. Synthesis Routes for Enhanced Piezoelectric Properties in Spark Plasma Sintered Ta-Doped KNN Ceramics. *J. Eur. Ceram. Soc.* **2022**, *42* (5), 2188−2194.
(21) Trepakov, V. A.; Savinov, M. E.; Železný, V.; Syrnikov, P. P.; Deyneka, A.; Jastrabik, L. Li Doping Effect on Properties and Phase Transfomations of $KNbO_3$. *J. Eur. Ceram. Soc.* **2007**, *27* (13−15), 4071−4073.
(22) Burns, S. R.; Dolgos, M. R. Sizing up $(K_{1-x}\,Na_{\,x})NbO_{\,3}$ Films: A Review of Synthesis Routes, Properties & Applications. *New J. Chem.* **2021**, *45* (17), 7408−7436.
(23) Song, G.; Song, Y.; Su, J.; Zhang, K.; Xing, L.; Yang, H.; Zhang, N. High Temperature Dielectric Properties and Magnetic Behavior of $K_{1-x}Ca_xNbO_3$ Ceramic. *Phys. B* **2021**, *602*, No. 412593.
(24) Durugkar, P. D.; Katpatal, A. G. Growth and Characterization of Pure, and Doped Crystals of Potassium Niobate. *J. Cryst. Growth* **1996**, *162* (3−4), 161−166.
(25) Dudhe, C. M.; Khambadkar, S. J. Oxygen Vacancy Dependent Structural Phases in KNbO 3. *Mater. Lett.* **2018**, *216*, 97−100.
(26) Kawamura, S.; Magome, E.; Moriyoshi, C.; Kuroiwa, Y.; Taniguchi, N.; Tanaka, H.; Maki, S.; Takata, M.; Wada, S. Electronic Polarization in $KNbO_3$ Visualized by Synchrotron Radiation Powder Diffraction. *Jpn. J. Appl. Phys.* **2013**, *52* (9), No. 09KF04.
(27) Hewat, A. W. Cubic-Tetragonal-Orthorhombic-Rhombohedral Ferroelectric Transitions in Perovskite Potassium Niobate: Neutron Powder Profile Refinement of the Structures. *J. Phys. C: Solid State Phys.* **1973**, *6* (16), 2559−2572.
(28) Zhou, L.; Bai, Z.; Wang, G.; Li, J.; Jin, M.; Zhang, X.; Peng, H.; Zhao, H.; Fan, Q.; Zhou, J.; Pan, X. Perovskite $KNbO_3$ Nanostructure for High-Response Photoelectrochemical Ultraviolet Detector. *J. Mater. Sci.: Mater. Electron.* **2023**, *34* (35), 2259.
(29) Wang, X.; Huan, Y.; Ji, S.; Zhu, Y.; Wei, T.; Cheng, Z. Ultra-High Piezoelectric Performance by Rational Tuning of Heterovalent-Ion Doping in Lead-Free Piezoelectric Ceramics. *Nano Energy* **2022**, *101*, No. 107580.
(30) Goodenough, J. B. Electronic and Ionic Transport Properties and Other Physical Aspects of Perovskites. *Rep. Prog. Phys.* **2004**, *67* (11), 1915−1993.
(31) Tomboc, G. M.; Zhang, X.; Choi, S.; Kim, D.; Lee, L. Y. S.; Lee, K. Stabilization, Characterization, and Electrochemical Applications of High-Entropy Oxides: Critical Assessment of Crystal Phase−Properties Relationship. *Adv. Funct. Mater.* **2022**, *32* (43), No. 2205142.
(32) Zhang, X.; Qi, R.; Dong, S.; Yang, S.; Jing, C.; Sun, L.; Chen, Y.; Hong, X.; Yang, P.; Yue, F.; Chu, J. Modulation of Ferroelectric and Optical Properties of La/Co-Doped $KNbO_3$ Ceramics. *Nanomaterials* **2021**, *11* (9), 2273.
(33) Yan, L.; Rui, X.; Chen, G.; Xu, W.; Zou, G.; Luo, H. Recent Advances in Nanostructured Nb-Based Oxides for Electrochemical Energy Storage. *Nanoscale* **2016**, *8* (16), 8443−8465.
(34) Come, J.; Augustyn, V.; Kim, J. W.; Rozier, P.; Taberna, P.-L.; Gogotsi, P.; Long, J. W.; Dunn, B.; Simon, P. Electrochemical Kinetics of Nanostructured Nb_2O_5 Electrodes. *J. Electrochem. Soc.* **2014**, *161* (5), A718−A725.
(35) Zhang, Q.; Ma, S.; Wang, W.; Gao, S.; Ou, Y.; Li, S.; Liu, X.; Lin, C. Zero-Strain" K2SrV4O12 as a High-Temperature Friendly Li^+-Storage Material. *Energy Storage Mater.* **2022**, *52*, 637−645.
(36) Wu, J.; Liu, H.-W.; Tang, A.; Zhang, W.; Sheu, H.-S.; Lee, J.-F.; Liao, Y.-F.; Huang, S.; Wei, M.; Wu, N.-L. Unexpected Reversible

https://doi.org/10.1021/acs.chemmater.4c02869
Chem. Mater. 2025, 37, 3100−3112

Crystalline/Amorphous (de)Lithiation Transformations Enabling Fast (Dis)Charge of High-Capacity Anatase Mesocrystal Anode. *Nano Energy* **2022**, *102*, No. 107715.
(37) Huang, Z.; Gao, H.; Yang, Z.; Jiang, W.; Wang, Q.; Wang, S.; Ju, J.; Kwon, Y.-U.; Zhao, Y. Improved Capacity and Cycling Stability of SnO_2 Nanoanode Induced by Amorphization during Cycling for Lithium Ion Batteries. *Mater. Des.* **2019**, *180*, No. 107973.
(38) Pecher, O.; Carretero-González, J.; Griffith, K. J.; Grey, C. P. Materials' Methods: NMR in Battery Research. *Chem. Mater.* **2017**, *29* (1), 213−242.
(39) Grey, C. P.; Dupré, N. NMR Studies of Cathode Materials for Lithium-Ion Rechargeable Batteries. *Chem. Rev.* **2004**, *104* (10), 4493−4512.
(40) Kuhn, A.; Pérez-Flores, J. C.; Hoelzel, M.; Baehtz, C.; Sobrados, I.; Sanz, J.; García-Alvarado, F. Comprehensive Investigation of the Lithium Insertion Mechanism of the $Na_2Ti_6O_{13}$ Anode Material for Li-Ion Batteries. *J. Mater. Chem. A* **2018**, *6* (2), 443−455.
(41) Calvez, E. L.; Dupré, N.; Gautron, É.; Douard, C.; Crosnier, O.; Brousse, T. Effect of Particle Microstructure and the Role of Proton on the Lithium Insertion Properties of HTiNbO5 Electrode Material. *Electrochim. Acta* **2023**, *455*, No. 142432.
(42) He, Y.-B.; Liu, M.; Huang, Z.-D.; Zhang, B.; Yu, Y.; Li, B.; Kang, F.; Kim, J.-K. Effect of Solid Electrolyte Interface (SEI) Film on Cyclic Performance of $Li_4Ti_5O_{12}$ Anodes for Li Ion Batteries. *J. Power Sources* **2013**, *239*, 269−276.
(43) De Luna, Y.; Bensalah, N. Mechanochemical Synthesis of Orthorhombic Nickel Niobate ($NiNb_2O_6$) as a Robust and Fast Charging Anode Material for Lithium-Ion Batteries. *ACS Appl. Energy Mater.* **2022**, *5* (6), 7443−7457.
(44) Liu, S.; Zhou, J.; Cai, Z.; Fang, G.; Pan, A.; Liang, S. Nb_2O_5 Microstructures: A High-Performance Anode for Lithium Ion Batteries. *Nanotechnology* **2016**, *27* (46), No. 46LT01.
(45) Yan, T.; Ding, R.; Ying, D.; Huang, Y.; Huang, Y.; Tan, C.; Sun, X.; Gao, P.; Liu, E. An Intercalation Pseudocapacitance-Driven Perovskite $NaNbO_3$ Anode with Superior Kinetics and Stability for Advanced Lithium-Based Dual-Ion Batteries. *J. Mater. Chem. A* **2019**, *7* (40), 22884−22888.
(46) Wang, T.; Ge, T.; Shi, S.; Wu, M.; Yang, G. Synthesis of Wolframite $FeNbO_4$ Nanorods as a Novel Anode Material for Improved Lithium Storage Capability. *J. Alloys Compd.* **2018**, *740*, 7−15.
(47) Diao, C. L.; Zheng, H. W. The Preparation and Surface Photovoltage Characterization of $KNbO_3$ Powder. *J. Mater. Sci.: Mater. Electron.* **2015**, *26* (5), 3108−3111.

https://doi.org/10.1021/acs.chemmater.4c02869
Chem. Mater. 2025, 37, 3100−3112